International Journal of Thermophysics (2023) 44:84
https://doi.org/10.1007/s10765-023-03184-4

PvT Properties and Thermodynamic Property Correlations for the Low Global Warming Potential Hydrofluoroolefin Refrigerant R-1132a (1,1-Difluoroethene)

Uthpala Perera[1] · Kozue Miyane[1] · Naoya Sakoda[1,2] · Kyaw Thu[1,3] · Yukihiro Higashi[1]

Received: 8 February 2023 / Accepted: 3 March 2023 / Published online: 17 April 2023

Abstract

R-1132a is increasingly being considered as a low global warming potential component in alternative mixtures to R-23 in specialized low temperature and ultra-low temperature refrigeration systems. Though the thermodynamic properties of R-1132a were investigated in several studies up to 2018, reinvestigations have been carried out in recent years. In order to contribute toward these renewed measurements, the critical parameters of R-1132a were experimentally re-determined. Thirty-two vapor pressures from 240 K to the critical temperature, fifteen saturated vapor and six saturated liquid densities above 254 K and the *PvT* properties in both the vapor phase (98 points) and liquid phase (34 points) from densities of 50 $kg{\cdot}m^{-3}$ to 760 $kg{\cdot}m^{-3}$ were also measured. Specific correlations for each of these properties were optimized and compared to previously available data from the literature. Additionally, the Peng–Robinson equation of state was used to represent the aforementioned properties and further utilized to determine the enthalpy and entropy of R-1132a.

Keywords Hydrofluoroolefin · Low GWP refrigerant · Low temperature refrigeration · R-1132a · R-23 alternative, Thermodynamic properties · Ultra-low temperature refrigeration

✉ Uthpala Perera
uthpala.perera@i2cner.kyushu-u.ac.jp

[1] Research Center for Next Generation Refrigerant Properties (NEXT-RP), International Institute for Carbon-Neutral Energy Research (I2CNER), Kyushu University, Fukuoka 819-0395, Japan

[2] Department of Mechanical Engineering, Kyushu University, Fukuoka 819-0395, Japan

[3] Interdisciplinary Graduate School of Engineering Sciences (IGSES), Kyushu University, Fukuoka 816-8580, Japan

1 Introduction

Among the pure hydrofluorocarbons (HFCs) currently being used by the heating, ventilation, air-conditioning and refrigeration (HVAC&R) industry, R-23 (trifluoromethane) has the highest global warming potential (GWP) which is 14,800 times that of CO_2 [1]. This refrigerant is mainly used either in pure form or in mixtures for specialized applications in the refrigeration sector, catering to low temperature (LT) and ultra-low temperature (ULT) refrigeration systems which can reach temperatures of − 40 °C to − 80 °C. These low temperatures are typically utilized in specialized laboratory and medical applications such as for the storage and transport of COVID-19 vaccines [2]. Under the Kigali amendment, R-23 is classified in Annex F-Group II, where it is considered as a byproduct of the production of R-22 and does not fall under the typical phase down schedule of other HFCs such as R-32, R-134a and R-125. However, considering the transition of the HVAC&R industry toward using low GWP refrigerants, replacing R-23 with a more favorable low GWP alternative seems imminent and essential in reducing HFC-related emissions. However, the lack of widely commercialized R-23 alternatives limits this transition. Recently, R-1132a, a pure hydrofluoroolefin (HFO), is being considered as a component in mixtures with high potential for replacing R-23, R-508, R-170 and similar refrigerants used in LT and ULT refrigeration systems [3, 4]. The low GWP value (< 3 [5]) of R-1132a coupled with its lower flammability compared to ASHRAE A3 hydrocarbons makes it an attractive option for the future. R-1132a was also identified as one of the few remaining pure refrigerants which fit several suitable thermodynamic properties and modeled performance characteristics as a low GWP next-generation refrigerant [6]. Several studies on refrigerant mixtures containing R-1132a have also been recently presented by Webster et al. [7], MacNeill et al. [8], Winkler et al. [9] and Perera et al. [10], which highlight its potential as a component in future low GWP refrigerant mixtures.

As for the thermodynamic properties of R-1132a, Mears et al. [11] presented several thermodynamic properties of pure R-1132a in 1955, where several techniques were used to measure the *PvT* properties in the vapor and liquid phases, vapor pressures, saturated liquid and vapor densities, critical parameters and liquid viscosities. Otto and Thomas [12] in 1964, presented the *PvT* properties mostly in the subcooled and supercritical regions, the vapor pressures, the saturated densities and the critical parameters. Koschine and Lehmann [13] measured the second and third virial coefficients for three isotherms in 1992, and Dymond et al. [14] presented the second virial coefficients and correlations in 2002. The next complete investigation on R-1132a was carried out by Low [5] in 2018. Low measured the vapor pressures, saturated densities, critical parameters and heat capacities. Low used these data to formulate a preliminary equation of state (EoS) and presented the final data as calculations based on the developed EoS. Additionally, Low conducted material compatibility tests, stability and flammability tests. The most recent investigations related to R-1132a are from Tomassetti and di Nicola [15], where the vapor pressures and superheated vapor-phase

PvT properties were measured and by Tomassetti et al. [16] where the triple-point temperature was presented. Thu et al. [17] recently published the vapor pressures along a single isochore in the two-phase region as well.

Till now, an international standard EoS for R-1132a has not been presented in the literature. One limiting factor is the lack of multiple sources of overlapping thermodynamic data to ensure the accuracy and validity of measurements. Gimenez-Prades et al. [3] recently pointed out that the data for R-1132a are still scarce and more accurate data are required for the development of an EoS for R-1132a. Similar conclusions on the lack of data on R-1132a were pointed out by Mota-Babiloni et al. [4] in a review on ULT systems. The lack of thermodynamic data has also restricted the experimental performance evaluations of R-1132a which is an essential step in testing its suitability for LT and ULT systems. In order to contribute to the improved information on R-1132a, several thermodynamic properties of R-1132a were measured in this work, then correlated and compared to the previously available literature. Additionally, the Peng–Robinson (P-R) EoS was used for calculating the aforementioned properties as well as the extended thermodynamic properties of R-1132a. These findings are presented in the following sections.

2 Experimental Section

2.1 Isochoric Apparatus

The vapor pressures, critical pressure and single-phase *PvT* properties of R-1132a were all measured using the isochoric method. The isochoric method involves the use of an 'isochoric apparatus' which consists of a constant volume cell directly connected to a pressure transducer which is immersed in a thermostatic bath. The bath temperature which is measured using a thermometer can be varied, and the pressure (P) and temperature (T) of the refrigerant sample can be measured at the desired conditions. By additionally knowing the sample mass (m) and inner volume of the cell (V_i), the sample density ($\rho = m/V_i$) or specific volume (v) can also be calculated to obtain *PvT* measurements along isochores. Three isochoric apparatus were utilized for the experimental measurements in this work. All three devices are previously described in detail and are referred to as 'Apparatus-Higher than Room Temperature' (App-HRT) [18], 'Apparatus-Lower than Room Temperature' (App-LRT) [19] and 'Apparatus-Wide Range of Temperatures' (App-WRT) [17]. All three apparatus have an upper pressure limit of 7 MPa.

The measurements begin with the cryogenic charging of a required mass of refrigerant (m) which has been gravimetrically measured using an electronic mass balance and has been explained in detail in the literature [19]. Once the refrigerant is charged, the isochoric cell together with the pressure transducer is immersed in the thermostatic bath where silicone oil is used as the thermal medium. The desired temperature values are input either in terms of resistance ratio using ITS-90 or in terms of Celsius through the data acquisition and control unit. A standard platinum resistance thermometer is used to measure the temperature of the bath, and sufficient time is allowed for thermal stability which is signified by the stability of the temperature

as well as the pressure readings. Finally, the pressure (P) readings are recorded together with the temperature (T) values. This process is repeated for another set point temperature until the required points along the isochore are measured.

The final expanded uncertainty is calculated for all measured parameters. For a measured parameter x with a 95 % ($k=2$) coverage factor, the expanded uncertainty $\left(U_x\right)$ is given in Eq. 1

$$U_x = k \cdot u_x\big|_{k=2}, \tag{1}$$

where k is the coverage factor and u_x is the combined standard uncertainty which is given in Eq. 2

$$u_x = \sqrt{s_x^2 + b_x^2}. \tag{2}$$

The combined standard uncertainty (u_x) consists of the statistical term (s_x) which accounts for the random errors caused by the fluctuations in raw data, while b_x accounts for the Type-B errors which include the instrument errors. For the measured parameters of temperature, pressure, volume and density, the final expanded uncertainties (U_x) for the three apparatus with a coverage factor of ($k=2$) are provided in Table 1. The schematics and detailed uncertainties for App-HRT and App-LRT and App-WRT have been provided in the literature [17–19].

2.2 Critical Point Apparatus

The 'critical point apparatus' (App-Crit) which has been previously described [20, 21] was used to measure both the critical temperature and density of R-1132a as well as the saturation densities near the critical point.

The principle behind these measurements includes the direct observation of the meniscus disappearance level as well as the critical opalescence phenomena which occur near the critical point. The main components of the apparatus consist of three pressure vessels, i.e., supplying vessel, expansion vessel and optical cell. These three vessels are interlinked with isolation valves and mounted on a rocking stage (for agitation and maintaining homogeneity of the sample). These vessels are immersed in a thermostatic bath with silicone oil. Temperature was measured with a 25 Ω standard platinum resistance thermometer calibrated against ITS-90. The sample density was calculated from the sample mass and inner volume.

One of the main advantages of this apparatus is its ability to use an initial mass of refrigerant charged into the system to measure multiple points of variable density values along the coexistence curve. This is achieved by decreasing the sample density by removing a fixed amount of sample (evacuation) and the expansion of the remaining sample either between the optical cell and expansion cell (secondary expansion) or across the three vessels (primary expansion). The detailed process and apparatus descriptions are provided in the literature [20, 21].

The experimental uncertainties ($k=2$) for the measured saturation conditions are dependent on the number of expansions used for changing the sample density. By limiting the number of expansions, the uncertainties in density have been kept below

Table 1 Final expanded uncertainties for the temperature (U_T), pressure (U_P), inner volume (U_V) and density (U_ρ) of the three isochoric apparatus

Property	App-HRT [18]	App-LRT [19]	App-WRT [17]
Temperature range/K	300–410	240–310	240–410
Pressure range	< 7 MPa		
Temperature control method	Heating coil with digital indicating controller	Internal heating coil and cooling unit with automated control	Heating coil with digital indicating controller + External constant cooling load
Temperature set point precision/mK	1	10	1
Thermostatic bath temperature distribution control	Mechanical stirrers ×8	Mechanical stirrer × 1 + Fluid pump × 1	Mechanical stirrers ×8
U_T / mK	10	30	10
U_P / kPa	1	1	1
U_V / cm^3	0.07	0.12	0.08
U_ρ / kg·m^{-3}	0.0015·ρ	0.003·ρ	0.002·ρ

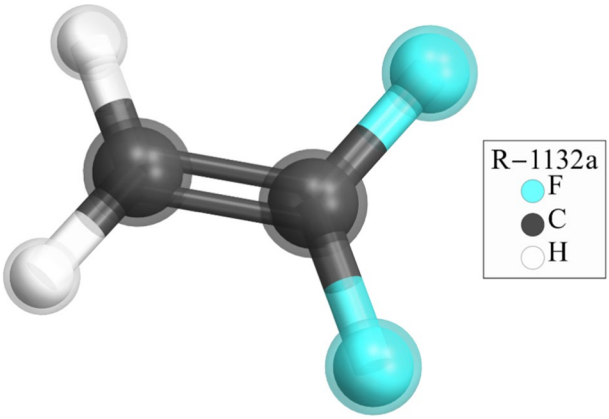

Fig. 1. 3D molecular structure of R-1132a obtained using Mathematica [29]

Table 2 Information and properties of the pure refrigerant R-1132a

Parameter	Value
Molecular formula	$C_2H_2F_2$
IUPAC chemical name	1,1-difluoroethene
CAS No	75-38-7
Molecular mass/g·mol^{-1}	64.0341 [30]
ASHRAE Std. 34 Name	A2 [31]
ASHRAE Std. 34 class	R-1132a [31]
ODP	0 [3]
GWP	< 3 [5]
Sample purity (mass%)	> 99.95
Supplier	Daikin Industries Ltd

0.3 %, while the temperature measurements have an uncertainty of $U_T = 10$ mK. The uncertainty at the critical point varies slightly from this due to the larger uncertainties associated with critical opalescence phenomena and difficulty in distinguishing the disappearance of the meniscus level. These uncertainties are reported together with the new critical parameters of R-1132a.

2.3 Refrigerant

The refrigerant R-1132a (CAS No. 75-38-7, 1,1-difluoroethene) belongs to the HFO family and has a carbon = carbon double bond. It only contains the elements of carbon, fluorine and hydrogen as seen in Fig. 1. A summary of several properties of R-1132a is provided in Table 2. The high-purity sample used in this work was provided by Daikin Industries Ltd. The sample purity is reported by manufacturers as more than 0.9995 in mass fraction. Additional purification was not carried out.

The thermodynamic properties of R-1132a presented within this work include: the critical temperature and density measured using the meniscus observation method; the critical pressure directly measured using an isochoric apparatus at the new critical point (and verified using another isochoric apparatus); the saturated vapor pressures measured using three isochoric apparatuses; the saturated liquid and vapor densities determined using the direct observations of meniscus disappearance near the critical point and using the inflection points of the *PvT* isochores; the *PvT* properties in the vapor and liquid phases measured along several isochores. Individual correlations were optimized for each of these properties. These correlations were also compared to previous measurements of R-1132a properties from the literature sources of Mears et al. [11], Otto and Thomas [12], Low [5], Tomassetti and di Nicola [15] and Thu et al. [17]. Additionally, the P-R EoS was utilized to represent the overall thermodynamic behavior of R-1132a and to obtain its enthalpy and entropy.

3 Results and Discussion

3.1 Critical Temperature and Density

The critical temperature and density were measured using the App-Crit. Both the observations of the disappearance of the meniscus as well as the intensity of the critical opalescence phenomena were taken into consideration. Through several evacuations and expansions, saturated densities near the critical point were observed.

A sample with a density of 429.9 $kg{\cdot}m^{-3}$ had a meniscus level at the center of the optical cell at room temperature. When the temperature of the thermostatic bath was increased, the meniscus level rose slightly. At a certain temperature, the meniscus began to show a change in color to a light yellow (critical opalescence). With increasing temperature, the liquid phase began to change in color and the meniscus intensity also increased to a dark brown and finally disappeared at 302.601 K. This was the first measurement determined to be near the critical point. Since the meniscus level was above the center level and the meniscus showed the critical opalescence, this point was determined to be located in the saturated liquid phase with a higher density than the critical value.

Next the density of 404.6 $kg{\cdot}m^{-3}$ was measured, with the meniscus level at room temperature being located similarly at the center level. As the temperature was increased, the meniscus level dropped very slightly and started to change color (light yellow), signifying the critical opalescence phenomena. Though initially the two phases above and below the meniscus remained clear, the vapor and liquid phases both started to change color together with the increasing of intensity of the meniscus at higher temperatures. Finally, the meniscus was almost completely opaque and it disappeared at 302.620 K, leaving behind an indistinguishable phase. Since the meniscus level was located slightly below the center as it disappeared, the sample was determined to be in the saturated vapor phase (lower density than the critical density). However, this sample was determined to be very close to the critical point

due to the intensity of the observed critical opalescence in both the meniscus and two phases.

Additionally, the lower density of 340.3 kg·m^{-3} was also measured, and the meniscus level at room temperature was much lower than the previous sample. With increasing temperature, the meniscus level continued to drop till it hit the bottom of the optical cell and disappeared at 302.051 K (saturated vapor). This point was clearly on the saturated vapor curve with a density much lower than the critical density.

Through these measurements and the observations of the meniscus level and critical opalescence, the critical density was determined to have a value higher than 404.6 kg·m^{-3} and lower than 429.9 kg·m^{-3}. The critical temperature should be between 302.620 K and 302.601 K. Based on the level at which the meniscus disappeared and the intensity of the critical opalescence of both the meniscus and the vapor and liquid phases, the critical density of R-1132a was determined as

$$\rho_c = 414 \pm 5 \text{ kg} \cdot \text{m}^{-3}. \tag{3}$$

Based on the slope of the coexistence curve near the critical point together with the temperatures of the saturated liquid and saturated vapor points mentioned above, the critical temperature of R-1132a was determine to be

$$T_c = 302.62 \pm 0.01\text{K}. \tag{4}$$

3.2 Critical Pressure

Using the above critical density, a sample at 413.8 ± 0.6 kg·m^{-3} was prepared and charged into the App-HRT. The isothermal bath temperature was increased to the critical temperature of 302.62 K and allowed to stabilize. The critical pressure was directly measured and is given below with an expanded uncertainty including a 95 % coverage factor ($k = 2$),

$$P_c = 4448 \pm 2\text{kPa}. \tag{5}$$

The new measurements for the critical temperature, density and pressure are summarized in Table 3 and compared with the previous values from the literature as well as predictions using group contributions. The Ambrose group contribution method was chosen since it could predict all three parameters and it had the smallest combined errors based on the previous work [19, 22].

The newly determined critical temperature is around 0.1 % lower than the values provided previously in the literature by Otto and Thomas [12] and Low [5] and is 0.2 % lower than those by Mears et al. [11]. The experimental uncertainty of the temperature measurement at the critical point of the present work is 0.01 K; Mears et al.'s uncertainty is 0.5 K, Low's [5] uncertainty was stated to be 0.3 K, while Otto and Thomas [12] optimized the critical parameter using a correlation for the saturation pressures. Therefore, the new measurement can be considered as an improved direct measurement of the critical temperature due to the smaller uncertainty and

Table 3 Critical parameters of R-1132a compared to the values in the literature and to the Ambrose empirical prediction based on group contributions

Critical parameter	Source	Value	Deviation	Deviation/%	Method
T_c/K	Present work	302.62	–	–	a
	Mears et al. [10]	303.25	0.63	0.21	b
	Otto and Thomas [11]	302.85	0.23	0.08	b
	Low [13]	302.81	0.19	0.06	c
	Ambrose [23]	301.32	− 1.3	− 0.43	d
ρ_c/kg·m^{-3}	Present work	414	–	–	a
	Mears et al. [10]	417	3	0.72	e
	Otto and Thomas [11]	414	0	0	e
	Low [13]	418	4	0.9	c
	Ambrose [23]	405	− 9	− 2.23	d
P_c/kPa	Present work	4448	–	–	f
	Present work	4447	− 1	− 0.03	g
	Mears et al. [10]	4433	− 15	− 0.33	h
	Otto and Thomas [11]	4463	15	0.34	h
	Low [13]	4461	13	0.29	i
	Ambrose [23]	4662	214	4.81	d

[a]Meniscus method (App-Crit)

[b]Meniscus method (sealed tube)

[c]Meniscus method (variable volume cell)

[d]Empirical equation (group contribution)

[e]Extrapolation of rectilinear diameter line (saturated densities)

[f]Direct measurement (App-HRT)

[g]Direct measurement (App-WRT)

[h]Extrapolation of vapor pressure equation

[i]Direct measurements (isochoric apparatus)

also since the values are within the uncertainty range of Low's measurements. The Ambrose method shows a higher deviation of 0.4 % from the expected values. The critical densities on the other hand are all within the experimental uncertainty of 5 kg·m^{-3}. The values provided by Otto and Thomas [12] are identical to the values measured by Higashi, while measurements by Low [5] differ by only 4 kg·m^{-3} and those by Mears et al. [11] differ by 3 kg·m^{-3}. The Ambrose method under-predicts the density by 9 kg·m^{-3}, which exceeds the uncertainty of the current experimental measurements, but is still relatively quite close to all three measurements from different sources. The similar measurements by four individual laboratories ensure the accurate representation of the critical density for R-1132a.

To ensure the reproducibility of the newly measured critical pressure using App-HRT, App-WRT was used to re-measure the critical pressure for a sample of $\rho = 414.3$ kg·m^{-3}. The two measurements were within 1 kPa or 0.03 %. This signifies the reproducibility of the measurement using a different apparatus as well

as the accuracy of the critical temperature and density. The R-1132a critical pressures previously provided in the literature by Mears et al. [11], Low [5] as well as Otto and Thomas [12] show around 0.3 % deviations from the current value, while the Ambrose method has much higher deviations reaching 5 %. Due to the lower temperature uncertainties as well as the similar values of the critical density value, the newly determined critical pressure within this work can be considered as an improved and updated direct measurement.

Overall, it was seen that the empirical methods based on group contributions would predict values which showed significant deviations to the experimentally determined critical points. Therefore, the use of direct critical point measurements with lower uncertainties will be beneficial for the improved development of an equation of state for R-1132a.

3.3 Optimized Correlations for the Thermodynamic Properties of R-1132a

3.3.1 Vapor Pressures in the Two-Phase Region along the Saturation Curve

The vapor pressures along the saturation line were measured using a critical isochore (App-WRT) in the temperature range of 260 K to 302.62 K (T_c) and several points near the critical point (including the critical pressure) using App-HRT. These measurements are given in Tables 4 and 5, respectively. In order to represent the newly measured saturation pressures, a Wagner type correlation [19] shown in Eq. 6 was optimized by minimizing the absolute average deviations in pressure (AAD_P) given in Eq. 9. In Eq. 6, the parameters *A*-*D* are constants, *T* is in Kelvin, *P* is in kPa, T_c is the new critical temperature, P_c is the new critical pressure and $\tau = \left(1 - T/T_c\right)$. The optimized parameters *A*-*D* together with the AAD_P are given in Table 6. In order to verify this new saturation pressure curve, App-LRT was used to measure the vapor

Table 4 Vapor pressures and sample density along the critical isochore up to the critical point using App-WRT

T/K	*P*/kPa	ρ/kg·m^{-3}
260.000	1567.82	414.67
260.000	1567.78	414.67
270.000	2051.77	414.51
270.000	2051.99	414.51
280.000	2638.93	414.34
280.000	2639.02	414.34
290.000	3344.95	414.18
290.000	3345.06	414.18
300.000	4194.86	414.01
300.000	4194.61	414.01
302.600	4444.66	413.97
302.620	4446.59[a]	413.97

[a]The critical pressure directly measured at the critical point

[b]The expanded uncertainties with coverage factor ($k=2$) are $U_T=10$ mK, $U_P=1$ kPa and $U_\rho=0.002\cdot\rho$ kg·m^{-3}

Table 5 Vapor pressures and sample density along the critical isochore near the critical point including the critical pressure measurement using App-HRT

T/K	P/kPa	ρ/kg·m^{-3}
295.079	3755.86	413.81
298.178	4028.00	413.86
300.001	4195.54	413.72
302.620[b]	4447.97[a,b]	413.67[b]

[a]The critical pressure directly measured at the critical point

[b]The expanded uncertainties for the critical point with a coverage factor ($k=2$) are $U_T=10$ mK, $U_P=2$ kPa and $U_\rho=5$ kg·m^{-3}

[c]The expanded uncertainties with coverage factor ($k=2$) are $U_T=10$ mK, $U_P=1$ kPa and $U_\rho=0.0015\ \rho$ kg·m^{-3}

Table 6 Optimized parameters for Eq. 6 and the AAD_P for representing the saturation pressure curve

A/–	B/–	C/–	D/–	AAD_P/%
– 6.8555	1.5762	– 1.8261	– 2.9966	0.007

Table 7 Vapor pressures and sample density along the saturation curve measured using App-LRT for verification of the optimized Wagner pressure correlation of Eq. 6

T/K	P/kPa	ρ/kg·m^{-3}
239.696	848.45	411.85
240.099	859.94	411.84
240.104	859.71	411.84
240.116	860.29	411.84
245.086	1008.29	411.77
250.202	1178.85	411.70
250.222	1179.45	411.70
255.113	1363.78	411.63
260.152	1573.63	411.56
260.152	1572.75	411.56
265.073	1799.97	411.49
270.094	2056.84	411.42
270.094	2055.88	411.42
275.137	2338.85	411.34
280.085	2641.96	411.27
285.026	2977.57	411.20

[a]The expanded uncertainties with coverage factor ($k=2$) are $U_T=30$ mK, $U_P=1$ kPa and $U_\rho=0.003\ \rho$ kg·m^{-3}

pressure in the two-phase region along an additional isochore in the temperature range of 240 K to 285 K (Table 7).

$$\ln P_{\mathrm{Calc}} = \ln P_{\mathrm{c}} + (T_{\mathrm{c}}/T_{\mathrm{Exp}})(A\tau + B\tau^{1.5} + C\tau^{2.5} + D\tau^{5}), \tag{6}$$

$$\Delta P = P - P_{\mathrm{Calc}}, \tag{7}$$

$$\Delta P[\%] = 100 \cdot \left(P - P_{\mathrm{Calc}}\right)/P_{\mathrm{Calc}}, \tag{8}$$

$$\mathrm{AAD}_P = \frac{\sum |\Delta P[\%]|}{N}. \tag{9}$$

Two-phase experimental vapor pressure data from the literature by Otto and Thomas [12], Tomassetti and di Nicola [15] and Thu et al. [17] and also vapor pressure data determined using the EoS developed by Low [5] were obtained for comparison. Though Tomassetti and di Nicola's data are the newest, it does not include a new measurement of the critical point and was limited to the range between 220 K and 280 K. The present measurements overlap Tomassetti and di Nicola's range starting from 240 K to 280 K and additionally provide higher temperature vapor pressures up to the critical pressure, overlapping those provided by Otto and Thomas and Low.

The vapor pressure measurements from the four groups were compared to the new Wagner correlation of Eq. 6 introduced within this work. Equation (6) is based on a majority of the *PT* data measured using App-WRT, several *PT* data near the critical point and the newly determined critical pressure measured using App-HRT as well as the critical temperature determined using App-Crit. The correlation is applicable within the temperature range of 260 K to the critical point based on the data used for optimization. The relative deviations of the vapor pressure in comparison with the optimized correlation are presented in Fig. 2.

As shown in Fig. 2, the new correlation reproduces the present data within adequate reproducibility since most of the deviations are within ± 0.1 %. The isochore which was used for verification purposes (measured using App-LRT) shows a good agreement with several measurements of App-WRT for temperature below 275 K. Additionally, the deviations from 240 K to 260 K (which is beyond the present

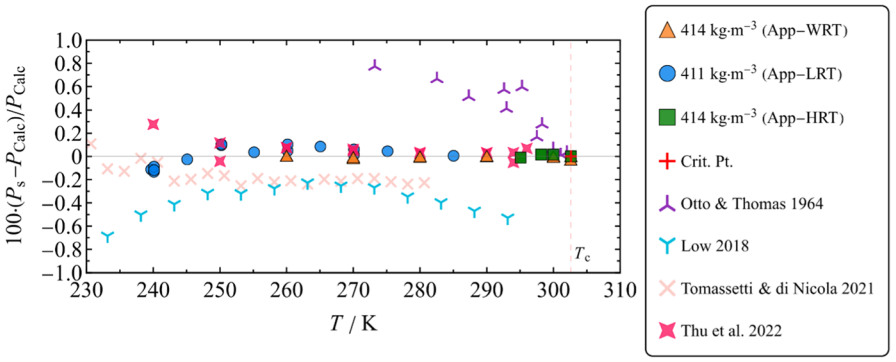

Fig. 2 Vapor pressure deviations in the two-phase region along the saturation pressure curve in comparison to the optimized correlation of Eq. 6: App-WRT; App-HRT; App-LRT; Otto and Thomas [12]; Low [5]; Tomassetti and di Nicola [15]; and Thu et al. [17]

correlation temperature range) are also within 0.1 %. The small deviations even at the extrapolated points suggest that the optimized correlation can accurately predict vapor pressures beyond the experimental range up to 240 K. The measurements from Thu et al. [17] also show similar deviations as expected; most data are within 0.1 % deviations, except for the low temperature point of 240 K, where they are slightly larger at 0.3 %. Higher relative deviations at lower temperatures are more acceptable, since the absolute pressure values are much smaller and hence amplify the effect on the relative deviations.

The measurements by Tomassetti and di Nicola [15] are around 0.2 % smaller for temperature above 240 K up to 280 K. At 240 K, the measurements show good consistency with both the measurements from App-LRT as well as the extrapolated correlation. The deviations below 240 K up to 230 K are distributed around the axis at deviations of around 0.1 %. They have an absolute deviation of less than 2 kPa which is similar in value to the experimental uncertainties.

The saturation pressure data provided by Low [5] are calculations based on Low's correlation and are not experimental measurements. These calculations are smaller than the new correlation in all instances. They have a distribution of deviations between 0.8 % and 0.2 %, with the largest deviations occurring near to the critical point and the lower temperatures. The higher deviations at both ends are expected. Toward the higher temperature end or nearer to the critical point, Low's correlation will be closer to their own critical point values. Since these critical points are different to those which are newly measured within this work, Low's calculations will show larger deviations near the critical point. The relative deviations can also increase at lower temperatures due to the smaller absolute pressures as mentioned before. The deviations between 250 K and 280 K are somewhat similar to the deviations for the data of Tomassetti and di Nicola. However, for lower temperatures, the data by Tomassetti and di Nicola are closer to the present measurements and correlation, than the data by Low.

The data by Otto and Thomas [12] have positive deviations in all instances, unlike the other data from the literature. The deviations reduce in value as they reach the new critical point. The measurements within this work and the correlation are located between the measurements by Otto and Thomas and those by Low. Tomassetti and di Nicola [15] commented on the consistency of the data by Otto and Thomas, due to the very large deviations in comparison to their results. Similar conclusions can be made in comparison to the present work, except nearer to the new critical point. It is interesting to note that the measurements by Otto and Thomas just below the critical point seem to be very similar to the measurements in this work and they seem to converge near the new critical point. However, the exact critical point provided by Otto and Thomas (based on the optimization of a correlation) is almost identical to the value of Low rather than the new measurements of this work.

3.4 Derivation of Additional Parameters Based on the Saturation Pressure Correlation

The acentric factor (ω) for R-1132a was provided by Low [5] as 0.181, and the normal boiling point (NBP) was also stated to be 190.34 K. Utilizing the new correlation in this work and the new critical parameters, a new acentric factor and NBP for R-1132a were calculated and compared. The acentric factor was calculated based on the equation provided by Pitzer et al. [23] given in Eq. 10, where temperature is $T = 211.834$ K, with a saturation vapor pressure of $P_{Sat} = 296.82$ kPa estimated through the extrapolation of the vapor pressure correlation Eq. 6. P_r is the reduced pressure with respect to the critical pressure $P_{c,}$ and T_r is the reduced temperature with respect to the critical temperature T_c.

$$\omega = -1 - \log P_r\big|_{T_r=0.7}. \tag{10}$$

The new acentric factor is 0.176, which is around 2.8 % lower than the value provided by Low. By utilizing the Wagner correlation, the NBP is determined when the pressure is 1 atm (101.325 kPa). The NBP = 189.85 K (− 83.30 °C), which is 0.49 K or 0.3 % smaller than the value reported by Low.

3.4.1 Coexistence Curve

The saturated densities were first presented by Otto & Thomas [12] and then by Low [5] for the temperature range of 273.15 K to 302.85 K and 193.15 K to 293.15 K and the density range of 92 kg·m^{-3} to 809 kg·m^{-3} and 4.91 kg·m^{-3} to 1099 kg·m^{-3}, respectively. The saturated densities in this work were measured using two methods in the temperature range of 254.52 K to 302.62 K and density range of 51.6 kg·m^{-3} to 757.0 kg·m^{-3} and are shown in Fig. 3. Firstly, App-Crit was used to measure the saturated densities and temperatures near the critical point. This method involved

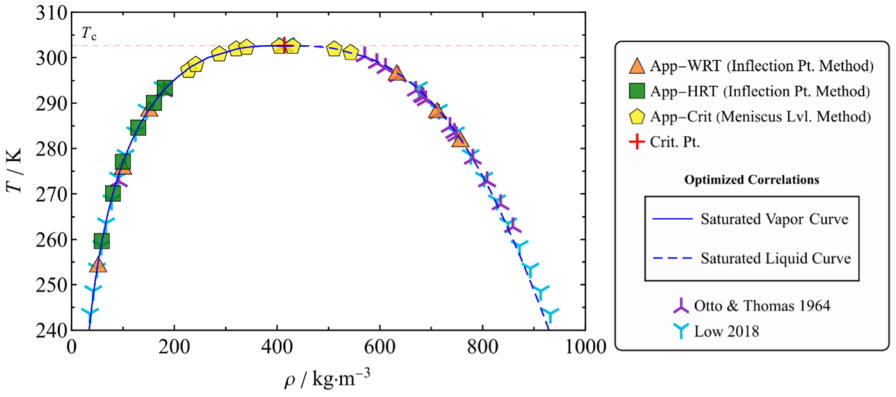

Fig. 3 Coexistence curve for R-1132a constructed using experimental measurements from both the direct meniscus measurement method and those derived through the inflection points of the *PvT* isochores, and the saturated densities obtained from Otto and Thomas [12] and Low [5]

Table 8 Saturation density and temperature data obtained using the critical point apparatus and the saturated pressures from Eq. 6

Saturated phase	ρ/kg·m^{-3}	U_ρ/kg·m^{-3}	T/K	P_{Calc}/kPa
Vapor	227.5	0.5	297.381	3956
	241.7	0.5	298.650	4070
	287.4	0.5	300.923	4282
	320.3	0.4	302.051	4391
	340.3	0.4	302.420	4428
	404.6	0.3	302.620[a]	4448
Liquid	429.9	0.3	302.601[a]	4446
	511.2	0.2	302.029	4389
	543.2	0.2	301.254	4314

[a]Critical opalescence was observed at these temperatures

[b]The expanded uncertainties with coverage factor ($k=2$) are $U_T=10$ mK and U_ρ are given above

Table 9 Saturation density and temperature data obtained using App-HRT and the inflection point method and the saturated pressures from Eq. 6

Saturated phase	ρ''/kg·m^{-3}	T/K	P_{Calc}/kPa
Vapor	58.9	259.63	1552
	80.6	270.12	2059
	99.9	277.06	2455
	129.8	284.60	2947
	160.2	290.05	3349
	181.5	293.40	3616

[a]The expanded uncertainties with coverage factor ($k=2$) are $U_\rho=0.0015\ \rho$ kg·m^{-3}, $U_T=30$ mK and $U_P=2$ kPa

the observation of the meniscus level at room temperatures and the meniscus disappearance with the change in temperature [20].

The second method used the isochoric PvT data together with the saturation pressure curve of Eq. 6 to determine the inflection point which signifies the transition from the two-phase region to either the single-phase vapor region or the single-phase liquid region. This method allows a wide range of saturation data to be obtained away from the critical point, by using the PvT data. Special consideration was required in determining the inflection points of isochores with higher densities. This is due to the presence of PvT measurements in the supercritical region. The authors recommend that data in this region are ignored whenever possible, to provide a more accurate estimation of the inflection points. The omitted PvT data during these fittings are marked with a superscript 'a' in the PvT data tables in the next section.

The saturated densities, temperatures and pressure data are provided in Table 8 for the meniscus based method and Tables 9 and 10 for the inflection point based method. The meniscus method does not have a direct pressure measurement, and hence, pressure values are estimated using optimized Eq. 6. The exact pressure at the inflection points was also not directly measured and are also based

Table 10 Saturation density and temperature data obtained using App-WRT and the inflection point method and the saturated pressures from Eq. 6

Saturated phase	ρ/kg·m^{-3}	T/K	P_{Calc}/kPa
Vapor	51.6	254.49	1340
	100.2	275.99	2390
	151.1	288.76	3250
Liquid	633.1	296.78	3903
	711.5	288.46	3228
	757.0	282.05	2773

[a]The expanded uncertainties with coverage factor ($k=2$) are $U_\rho=0.002\,\rho$ kg·m^{-3}, $U_T=30$ mK and $U_P=2$ kPa

on the above correlation. The errors associated with each method are as follows: the meniscus method has expanded uncertainties ($k=2$) for temperature of $U_T=10$ mK and U_ρ for densities which are provided in Table 8 with the experimental data; the PvT inflection points have expanded uncertainties ($k=2$) for temperature, pressure and density of $U_T=30$ mK, $U_P=2$ kPa and $U_\rho=0.0015\cdot\rho$ kg·m^{-3} for App-HRT and $U_T=30$ mK, $U_P=2$ kPa and $U_\rho=0.002\cdot\rho$ kg·m^{-3} for App-WRT.

These data together with the critical parameters defined within this work were used to optimize a new coexistence curve [24]. A simplified five-term Guggenheim's equation [25] was chosen to represent the two saturated curves separately and is given in Eq. 11 representing the saturated liquid density (ρ') and Eq. 12 for the saturated vapor density (ρ''). The optimized coefficients for each phase together with the absolute average deviation in density (AAD_ρ) are given in Table 11. The deviations between the new correlation and the experimental data within this work and those by Otto and Thomas [12] and Low [5] are presented in Fig. 4.

$$\rho'(\rho_c,\tau)=\rho_c\left(1+B_1\tau^{1/3}+B_2\tau^{2/3}+B_3\tau+B_4\tau^{4/3}+B_5\tau^{5/3}\right), \tag{11}$$

Table 11 Optimized parameters for Eqs. 11 and 12 representing the coexistence curve along the saturated liquid and vapor states separately, their respective AAD_ρ and their applicable temperature and density ranges

Saturated liquid density (ρ') parameters for Eq. 11		Saturated Vapor density (ρ'') parameters for Eq. 12	
B_1	1.6363	C_1	-1.6099
B_2	2.0163	C_2	-1.9695
B_3	-3.0709	C_3	-3.5910
B_4	0.1658	C_4	-0.3869
B_5	2.5728	C_5	-0.8534
AAD_ρ/%	0.51	AAD_ρ/%	1.09
Density range/kg·m^{-3}	441 (ρ_c)–757	Density range/kg·m^{-3}	51.6–441 (ρ_c)
Temperature range/K	296.8–302.62 (T_c)	Temperature range/K	254.5–302.62 (T_c)

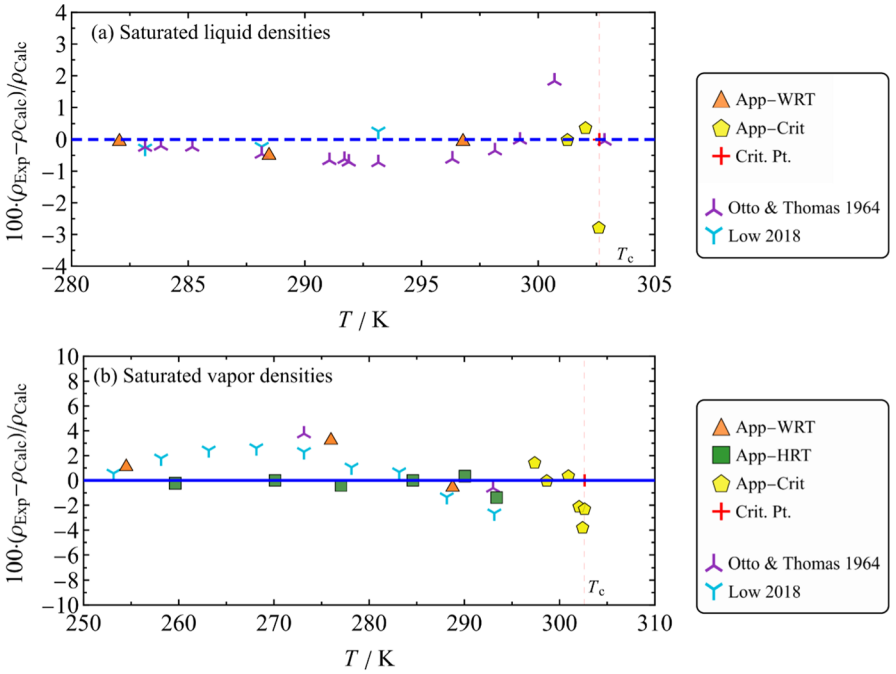

Fig. 4 Deviations in densities compared to (**a**) Eq. 11 for the saturated liquid densities and (**b**) Eq. 12 for the saturated vapor densities

$$\rho''(\rho_c, \tau) = \rho_c \cdot e^{\left(C_1\tau^{1/3}+C_2\tau^{2/3}+C_3\tau+C_4\tau^{4/3}+C_5\tau^{5/3}\right)}, \tag{12}$$

$$\Delta\rho = \rho - \rho_{\text{Calc}}, \tag{13}$$

$$\Delta\rho[\%] = 100 \cdot \left(\rho - \rho_{\text{Calc}}\right) / \rho_{\text{Calc}}, \tag{14}$$

$$\text{AAD}_\rho = \frac{\sum |\Delta\rho[\%]|}{N}. \tag{15}$$

The new correlation and measured data in the saturated liquid and vapor states match well with the previous results of Otto and Thomas [12] as well as those of Low [5] within the applicable density range shown in Table 11 as seen by the similar distributions of deviations in Fig. 4. The correlation has slightly higher deviations when representing data beyond the current experimental and temperature ranges, especially when compared to the results by Low. This is a typical characteristic observed when extrapolating beyond the experimental ranges. The data obtained using both the meniscus method and the *PvT* inflection points also show similar deviations, except for a few measurements nearer to the critical

point. The data in the saturated vapor phase near the critical point show slightly larger deviations. Due to the complexity of observing the exact point at which the meniscus disappears and the occurrence of critical opalescence, combined with the shape of the coexistence curve near the critical point, the higher density deviations for these points are acceptable.

3.4.2 *PvT* Properties in the Single Phase

The *PvT* properties in the single-phase regions were measured using App-HRT for temperatures above 300 K and using App-WRT for temperatures above 260 K. The isochores in the vapor phase consisted of six measurements using App-HRT with a

Table 12 *PvT* properties in the single-phase superheated vapor region measured using App-HRT

T/K	ρ/kg·m^{-3}	*P*/kPa	*T*/K	ρ/kg·m^{-3}	*P*/kPa	*T*/K	ρ/kg·m^{-3}	*P*/kPa
305.000	59.0	1951.19	305.000	100.1	2905.91	305.000	160.6	3825.48
310.000	59.0	1997.40	310.000	100.1	2993.32	310.000	160.5	3984.84
320.000	59.0	2088.92	320.000	100.1	3165.90	320.000	160.5	4297.36
330.000	58.9	2179.62	330.000	100.0	3335.88	330.000[a]	160.4	4603.27
340.000	58.9	2269.56	340.000	100.0	3503.63	340.000[a]	160.3	4903.96
350.000	58.9	2358.79	350.000	99.9	3669.66	350.000[a]	160.2	5200.56
360.000	58.9	2447.41	360.000	99.9	3834.03	360.000[a]	160.2	5493.53
370.000	58.8	2535.44	370.000	99.9	3996.86	370.000[a]	160.1	5783.37
380.000	58.8	2622.95	380.000	99.8	4158.37	380.000[a]	160.0	6070.53
390.000	58.8	2709.92	390.000	99.8	4318.66	390.000[a]	160.0	6354.98
400.000	58.7	2796.35	400.000[a]	99.7	4477.82	400.000[a]	159.9	6637.43
310.000	80.8	2560.02	305.000	130.1	3427.20	310.000	181.8	4222.01
320.000	80.7	2692.70	310.000	130.1	3548.97	320.000[a,b]	181.7	4587.02
330.000	80.7	2823.76	320.000	130.0	3788.52	330.000[a]	181.7	4943.83
340.000	80.7	2953.29	330.000	129.9	4023.62	340.000[a]	181.6	5294.39
350.000	80.6	3081.69	340.000	129.9	4255.20	350.000[a]	181.5	5639.85
360.000	80.6	3209.04	350.000[a]	129.8	4483.85	360.000[a]	181.4	5981.03
370.000	80.6	3335.26	360.000[a]	129.8	4709.83	370.000[a]	181.3	6318.68
380.000	80.5	3460.53	370.000[a]	129.7	4933.60	380.000[a]	181.2	6652.97
390.000	80.5	3585.00	380.000[a]	129.6	5155.35	305.000[a,c]	413.6	4681.24
400.000	80.4	3708.61	390.000[a]	129.6	5375.27	310.000[a,c]	413.5	5169.19
–	–	–	400.000[a]	129.5	5593.46	315.000[a,c]	413.4	5658.53
–	–	–	–	–	–	320.000[a,c]	413.3	6149.24
–	–	–	–	–	–	325.000[a,c]	413.3	6640.06

[a]Data in the supercritical region omitted when determining the *PvT* inflection points

[b]A single *PvT* data point in the supercritical region was required for determining the inflection point

[c]These data are the continuations of the critical isochore beyond the critical point (supercritical region)

[d]The expanded uncertainties with coverage factor ($k=2$) are $U_T=10$ mK, $U_\rho=0.0015\ \rho$ kg·m^{-3} and $U_P=1$ kPa

Table 13 *PvT* properties in the single-phase superheated vapor region measured using App-WRT

T/K	ρ/kg·m^{-3}	*P*/kPa	*T*/K	ρ/kg·m^{-3}	*P*/kPa	*T*/K	ρ/kg·m^{-3}	*P*/kPa
270.150	51.7	1458.29	280.150	100.3	2450.19	300.150	151.2	3569.13
280.150	51.7	1541.68	280.150	100.3	2450.55	300.150	151.2	3569.51
290.150	51.6	1623.22	290.150	100.3	2637.53	305.150	151.2	3719.38
300.150	51.6	1703.42	290.150	100.3	2637.98	305.150	151.2	3719.73
305.150	51.6	1743.09	300.150	100.2	2817.98	310.150	151.2	3867.15
310.150	51.6	1782.52	300.150	100.2	2818.38	310.150	151.2	3867.70
320.150	51.6	1860.72	305.150	100.2	2906.51	320.150	151.1	4157.23
330.150	51.6	1938.17	305.150	100.2	2906.93	320.150	151.1	4157.81
340.150	51.5	2014.93	310.150	100.2	2994.01	330.150[a]	151.0	4441.45
345.150	51.5	2053.10	310.150	100.2	2994.49	340.150[a]	151.0	4720.76
–	–	–	320.150	100.2	3166.70	340.150[a]	151.0	4721.18
–	–	–	330.150	100.1	3336.63	345.150[a]	150.9	4858.94
–	–	–	340.150	100.1	3504.30	–	–	–
–	–	–	345.150	100.1	3587.44	–	–	–

[a]Data in the supercritical region omitted when determining the *PvT* inflection points

[b]The expanded uncertainties with coverage factor ($k=2$) are $U_T=10$ mK, $U_\rho=0.002\ \rho$ kg·m^{-3} and $U_P=1$ kPa

density range of 60 kg·m^{-3} to 180 kg·m^{-3} and three measurements using App-WRT with the density range of 50 kg·m^{-3} to 150 kg·m^{-3}. The isochores in the liquid phase were measured only using App-WRT and consisted of three isochores in the density range of 630 kg·m^{-3} to 760 kg·m^{-3}. Additionally, a single isochore in the supercritical region as a continuation of the critical isochore was also measured using App-HRT. These *PvT* properties are presented in Tables 12 and 13. Previous measurements in the vapor phase were carried out by Tomassetti and di Nicola[15] with the densities being in the lower range (11 kg·m^{-3} to 76 kg·m^{-3}) and the temperature reaching 220 K. Otto and Thomas [12] carried out *PvT* measurements mostly in the liquid phase for the density range of 358 kg·m^{-3} to 897 kg·m^{-3} and for temperatures between 258 K and 343 K. Mears et al. [11] provided vapor-phase *PvT* in graphical form for the density range of 98 kg·m^{-3} to 212 kg·m^{-3} for temperature above 303 K.

3.4.3 *PvT* Properties in the Superheated Vapor Phase

The vapor-phase *PvT* properties shown in Tables 12 and 13 were correlated with the virial EoS truncated at the third term given in Eq. 16.

$$P = \frac{RT}{v}\left(1 + \frac{B}{v} + \frac{C}{v^2}\right). \tag{16}$$

Firstly, for each isotherm the second (B) and third (C) virial coefficients are obtained by minimizing the AAD_p at each temperature. The obtained B and C coefficients for each isotherm are given in Table 14. These B and C values are then used to optimize the temperature profiles for each coefficient in order to be able to obtain

Table 14 Second (B) and third (C) virial coefficients for experimental isotherms determined by minimizing the AAD_p and the B and C coefficients calculated using Eqs. 17 and 18

T/K	B/dm^3·mol^{-1}	C/dm^6·mol^{-2}	B_{Calc}/dm^3·mol^{-1}	C_{Calc}/dm^6·mol^{-2}
270.150	− 0.2531	0.0134	− 0.2533	0.0146
280.150	− 0.2361	0.0169	− 0.2340	0.0154
290.150	− 0.2187	0.0165	− 0.2165	0.0150
300.150	− 0.1998	0.0139	− 0.2004	0.0142
305.000	− 0.1912	0.0130	− 0.1931	0.0137
310.000	− 0.1838	0.0123	− 0.1859	0.0131
320.000	− 0.1707	0.0115	− -0.1723	0.0121
330.000	− 0.1587	0.0107	− 0.1598	0.0111
340.000	− 0.1477	0.0100	− 0.1482	0.0102
345.150	− 0.1447	0.0107	− 0.1426	0.0098
350.000	− 0.1372	0.0091	− 0.1375	0.0094
360.000	− 0.1278	0.0084	− 0.1275	0.0088
370.000	− 0.1192	0.0078	− 0.1182	0.0082
380.000	− 0.1112	0.0073	− 0.1095	0.0077
390.000	− 0.1046	0.0073	− 0.1014	0.0073
400.000	− 0.0978	0.0070	− 0.0938	0.0070

Table 15 Coefficients for the temperature-dependent function for representing the second virial coefficient B given in Eq. 17

b_0/dm^3·mol^{-1}	b_1/dm^3·K·mol^{-1}	b_2/dm^3·K^2·mol^{-1}
0.122515	− 55.3194	− 12486.2

Table 16 Coefficients for the temperature-dependent function for representing the third virial coefficient C given in Eq. 18

c_1/J·K^{-1}·mol^{-1}	c_2/J·K^{-1}·mol^{-1}	c_3/J·K^{-1}·mol^{-1}	c_4/J·K^{-1}·mol^{-1}
0.003693	0.344758	0.016502	− 0.021025
c_5/J·K^{-1}·mol^{-1}	c_6/J·K^{-1}·mol^{-1}	c_7/J·K^{-1}·mol^{-1}	c_8/J·K^{-1}·mol^{-1}
1.9626	− 4.24474	− 0.712908	0.093939

the relevant virial coefficient at any temperature. The temperature profiles are represented using Eqs. 17 and 18, where the optimized coefficients are obtained by minimizing the AAD_P. The AAD_P is minimized to 0.21 %, and the optimized coefficients for Eqs. 17 and 18 are given in Tables 15 and 16. The virial coefficients for each isotherm and the new temperature-dependent functions are shown in Fig. 5.

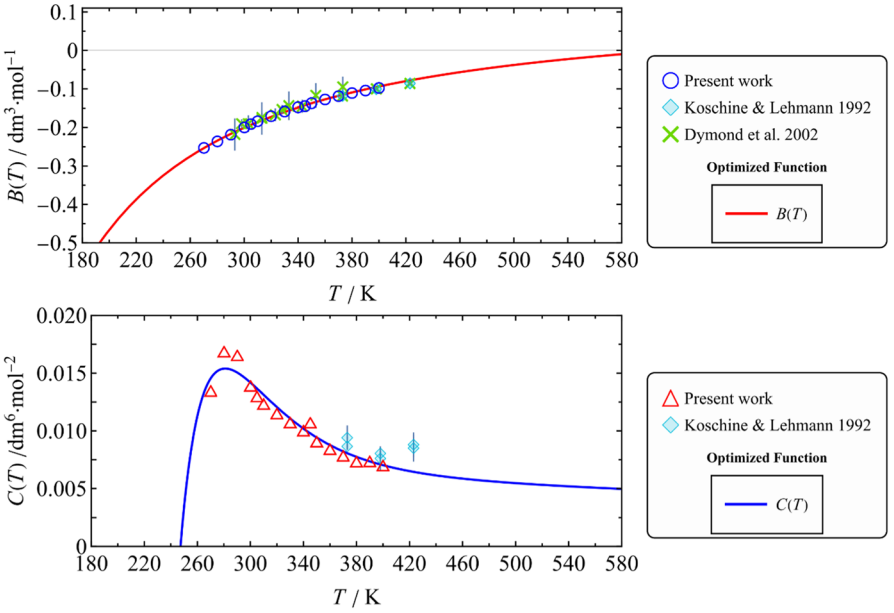

Fig. 5 Experimentally determined virial coefficients B and C with the optimized temperature dependence functions from Eqs. 17 and 18 as well as data from the literature: B of the present work; B of Koschine and Lehmann [13]; B of Dymond et al. [14]; B temperature-dependent function of the present work; C of the present work; C of Koschine and Lehmann [13]; and C temperature-dependent function of the present work

$$B(T) = b_0 + \frac{b_1}{T} + \frac{b_2}{T^2}, \tag{17}$$

$$C(T) = \frac{RT_c^2}{P_c^2}\left[\left(c_1 + \frac{c_2}{T_r^{2.8}} - \frac{c_3}{T_r^{10.5}}\right) + \omega\left(-c_4 + \frac{c_5}{T_r^{2.8}} + \frac{c_6}{T_r^3} - \frac{c_7}{T_r^6} - \frac{c_8}{T_r^{10.5}}\right)\right]. \tag{18}$$

The optimized temperature functions for $B(T)$ and $C(T)$ follow the expected trend [10] as seen in Fig. 5. The second virial coefficient experimental data obtained from Koshchine and Lehmann [13] and Dymond et al. [14] correspond well to both the experimental data determined in this work and to the new temperature-dependent function of Eq. 17. The shape of optimized Eq. 18 shows the expected peak near the critical point of R-1132a and slowly moves toward the origin as the temperature is increased. The availability of experimental data on either side of the critical point is beneficial in ensuring the proper fitting of C. The third virial coefficient data provided by Koschine and Lehmann are very close to the predicted curve except at 423 K which lies beyond the present experimental range. The general trend in the data from Koschine and Lehmann is slightly inconsistent when considering the high temperature point of 423 K as it increases in value when it is expected to decrease

with higher temperatures after the peak and thus can be ignored. Experimental data beyond the present experimental range in both the low temperature and high temperature regions would be further useful for verifying the new correlation and further improving it.

By using the temperature-dependent functions for $B(T)$ and $C(T)$, the virial EoS was used to determine the deviations in pressure for the PvT data in this work and those by Tomassetti and di Nicola [15] and Mears et al. [11] beyond the temperature and density range of the present data. The single vapor-phase isochore of Otto and Thomas [12] was excluded since it is in the supercritical phase. The data of Mears et al. [11] were not provided in tabular form and were extracted from graphical form and thus carry a slightly larger uncertainty. The deviations are shown in Fig. 6.

The data by Tomassetti and di Nicola [15] occupy lower densities and can be considered to be closer to the ideal gas state and are represented better with the virial EoS. The AAD_p for the data by Tomassetti and di Nicola increased very slightly to 0.22 % compared to the fitting carried out by Tomassetti and di Nicola which gave an AAD_p of 0.20 %. However, this increase is acceptable since the new fitting was purely optimized based on the data of the present work and it is still capable of providing similar deviations to those reported by Tomassetti and di Nicola. This illustrates the ability of the new virial coefficient functions to reproduce data from the literature which are beyond the fitting range.

The present data show somewhat larger deviations at higher temperatures since they have relatively higher densities and are further away from ideal gas behavior. However, the deviations are comparable to those of lower densities even at 350 K.

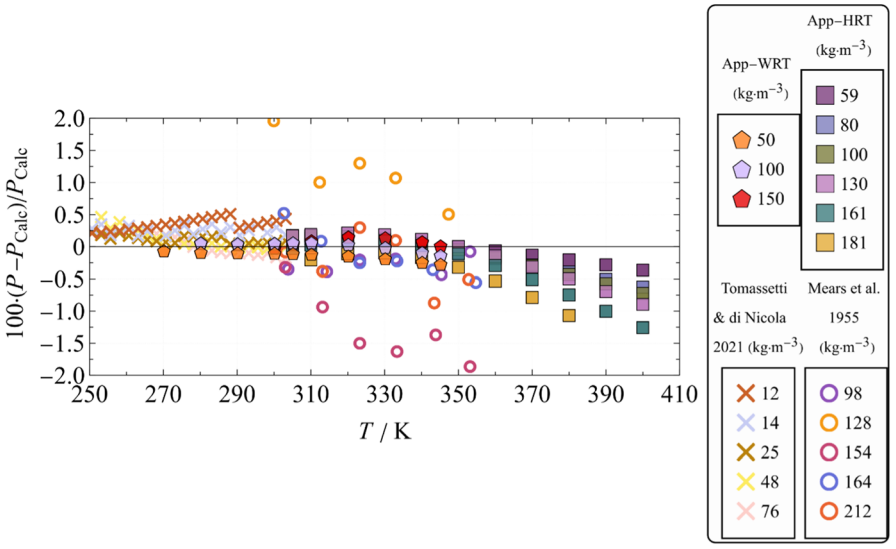

Fig. 6 Deviations in pressure of the single-phase superheated vapor PvT isochores from the virial EoS with optimized $B(T)$ and $C(T)$ coefficients of Eqs. 17 and 18. App-WRT isochores with densities: 50, 100, 150 kg·m^{-3}; App-HRT isochores with densities: 59, 80, 100, 130, 161 and 181 kg·m^{-3}; Tomassetti and di Nicola [15]: 12, 14, 25, 48 and 76 kg·m^{-3}; and Mears et al. [11]: 98, 128, 154, 164 and 212 kg·m^{-3}

The AAD_p for the present data is 0.21 % which is similar to the AAD_p obtained for Tomassetti and di Nicola's [15] data. Thus, the newly optimized virial coefficient functions can be used to reproduce data over a wider range of temperatures and densities.

Though the present data and the data by Tomassetti and di Nicola [15] show comparable deviations, the data by Mears et al. [11] show a wider distribution of deviations for several of its isochores. A trend similar to those seen above is not visible for these data, since the deviations do not correspond to the sample densities or temperature. The uncertainty in experimental data of Mears et al. was stated to be 2 kPa, while the extractions of data from graphical representation would also result in a slight increase in uncertainty. However, the AAD_p for Mears et al.'s data is 0.67 % which is much smaller than the AAD_p obtained when using Tomassetti and di Nicola's fitting. The fitting from Tomassetti and di Nicola was restricted to the second term of the virial EoS which results in a lower capacity to predict *PvT* properties for higher densities such as those of Mears et al. The new correlation for the vapor *PvT* properties could be considered as an improvement in the previous model due to the addition of the third virial coefficient and the wider applicable range.

3.5 Subcooled Liquid Densities

The Tait correlation given in Eq. 19 together with the β term in Eq. 20 is capable of using a combined form of the saturation pressure correlation (P_s) Eq. 6 and saturated

Table 17 Subcooled liquid-phase *PvT* properties measured using App-WRT

T/K	ρ/kg·m^{-3}	*P*/kPa	*T*/K	ρ/kg·m^{-3}	*P*/kPa	*T*/K	ρ/kg·m^{-3}	*P*/kPa
302.000	633.2	5025.38	290.000	711.6	3673.31	284.000	757.2	3438.91
302.000	633.2	5025.93	290.000	711.6	3674.56	284.000	757.2	3439.32
304.000[a,b]	633.1	5445.54	292.000	711.6	4236.87	286.000	757.1	4112.35
304.000[a,b]	633.1	5449.09	292.000	711.6	4238.19	286.000	757.1	4113.09
306.000[a]	633.1	5874.30	294.000	711.5	4804.74	288.000	757.0	4790.11
306.000[a]	633.1	5876.40	294.000	711.5	4806.70	288.000	757.0	4790.65
308.000[a]	633.0	6304.29	296.000	711.5	5376.69	290.000	757.0	5471.08
308.000[a]	633.0	6307.00	296.000	711.5	5378.00	290.000	757.0	5471.41
310.000[a]	633.0	6736.92	298.000	711.4	5952.72	292.000	756.9	6154.59
310.000[a]	633.0	6740.82	298.000	711.4	5953.69	292.000	756.9	6154.89
–	–	–	299.000	711.4	6242.01	–	–	–
–	–	–	299.000	711.4	6242.61	–	–	–
–	–	–	300.000	711.4	6531.69	–	–	–
–	–	–	300.000	711.4	6531.74	–	–	–

[a]Data in the supercritical region omitted when determining the *PvT* inflection points

[b]*PvT* data in the supercritical region was required for determining the inflection point

[c]The expanded uncertainties with coverage factor ($k=2$) are $U_\rho = 0.002 \cdot \rho$ kg·m^{-3}, $U_T = 10$ mK and $U_P = 1$ kPa

Table 18 Optimized parameters for Eqs. 19 and 20 for representing the subcooled liquid *PvT* isochores and the AAD_ρ of the fitting

a	*b*	*c*	*d*	*f*	AAD_ρ/%
− 0.55099	7.9777	0.15048	4.5732	3.2478	0.4

liquid density function (ρ') Eq. 11 to represent *PvT* properties in the subcooled liquid region. Its application is strictly limited to the subcooled liquid region and cannot represent properties in the supercritical region (beyond the critical temperature for liquid *PvT* isochores). Thus, the data which were used for fitting were limited to those with pressure and temperature pairs below the critical point. These subcooled liquid-phase *PvT* data are provided in Table 17 with the omitted data signified with the superscript '*a.*' The fitting process was carried out by reducing the error function of the AAD_ρ given in Eq. 15. The optimized coefficients *a*–*f* and AAD_ρ are given in Table 18.

$$\frac{1}{\rho} = \frac{1}{\rho'}\left[1 - c\ln\left(\frac{\beta + P}{\beta + P_s}\right)\right], \tag{19}$$

$$\beta = P_c\left(-1 + a\tau^{1/3} + b\tau^{2/3} + d\tau + f\tau^{4/3}\right). \tag{20}$$

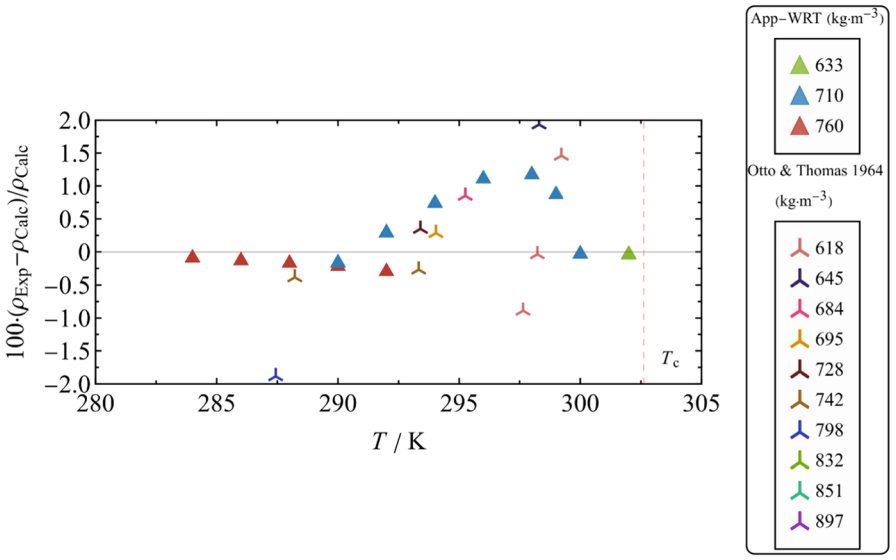

Fig. 7 Deviations in density of the single-phase subcooled liquid *PvT* isochores from optimized Eq. 19: App-WRT isochores of densities 633, 710 and 760 kg·m^{-3}, and isochores from Otto and Thomas [11] 618, 645, 684, 695, 728, 742, 798, 832, 851 and 897 kg·m^{-3}

The deviations for the predictions using Eq. 19 are presented in Fig. 7, with the results providing a AAD_{ρ} of 0.4 %. The measurements of Otto–Thomas [12] in the subcooled liquid region have also been included in the deviation plot. The scattering of deviations is similar to those measured within this work.

The 760 kg·m^{-3} isochore shows the smallest deviations. The deviations typically increase when the sample density approaches the critical density value. The deviations also typically increase with increasing temperature along an isochore as it moves away from the saturated conditions. The isochore of 710 kg·m^{-3} shows relatively large deviations almost reaching 1.5 %. The isochores of Otto and Thomas [12] with similar densities to those in this work show a similar trend. Therefore, the results within this work are corroborated through the measurements of Otto and Thomas. Several other isochores of Otto and Thomas (above the largest density of 760 kg·m^{-3} of this work) present larger deviations and have not been shown in the deviation plot above. Additionally, the isochore of 633 kg·m^{-3} which is very close to the supercritical region does not have adequate points below the critical temperature to show a trend in deviation.

3.6 Generalized Representation of R-1132a Using the Peng–Robinson Equation of State

The previous section provided specific correlations for individual properties at different phase conditions. These are important for scientists and researchers involved in property measurements and the development of equations of state for refrigerants as well as to verify the accuracy of the measurements. However, a more generalized representation of refrigerants is crucial for the industry and practical use. The P-R EoS [26] given in Eq. 21 has been extensively used for this purpose [27]. Therefore, the P-R EoS is used to represent R-1132a. This includes its saturation pressure curve, coexistence curve, *PvT* isochores in the single-phase regions and additionally the calculated pressure–enthalpy (*P–h*) properties and temperature–entropy (*T–s*) relationship. In order to utilize the P-R EoS, the following parameters are required: critical temperature, pressure and density (T_c, P_c and ρ_c), which were newly measured within this work; acentric factor (ω), which was determine using the optimized saturation pressure correlation, and the ideal gas specific heat capacity at constant pressure (c_P^{IG}) which was estimated using the Joback method [28] and is given in Eq. 22 as a function of temperature.

$$P = \frac{RT}{v-b} - \frac{a}{v(v+b)+b(v-b)}, \tag{21}$$

$$c_P^{IG} = -36.63 + 0.1974T + 1.43 \times 10^{-4} \cdot T^2 + 4.38 \times 10^{-8} \cdot T^3. \tag{22}$$

In Eqs. 21 and 22, P is the pressure in kPa, T is the temperature in K, v is the molar volume in m^3·mol^{-1}, a is the attraction term, and b is the repulsion term due to the volume of molecules as given by Peng and Robinson [26]. The P-R EoS was used to compare the measured properties within this work for the saturation pressures, saturated vapor density, saturated liquid density and both the vapor- and

Table 19 Comparison of absolute average deviations (AAD) of pressure or density for the optimized equations for each thermodynamic property relation and the P-R EoS

Thermodynamic property	Specific correlation		P-R EoS AAD/%
	Eqs.	AAD/%	
Vapor-phase (saturation) pressure (P_s)	6	0.01	0.34
Saturated liquid density (ρ')	11	0.51	13.74
Saturated vapor density (ρ'')	12	1.10	4.39
Superheated vapor pressure (P)	16	0.21	1.29
Subcooled liquid density (ρ)	19	0.40	18.94

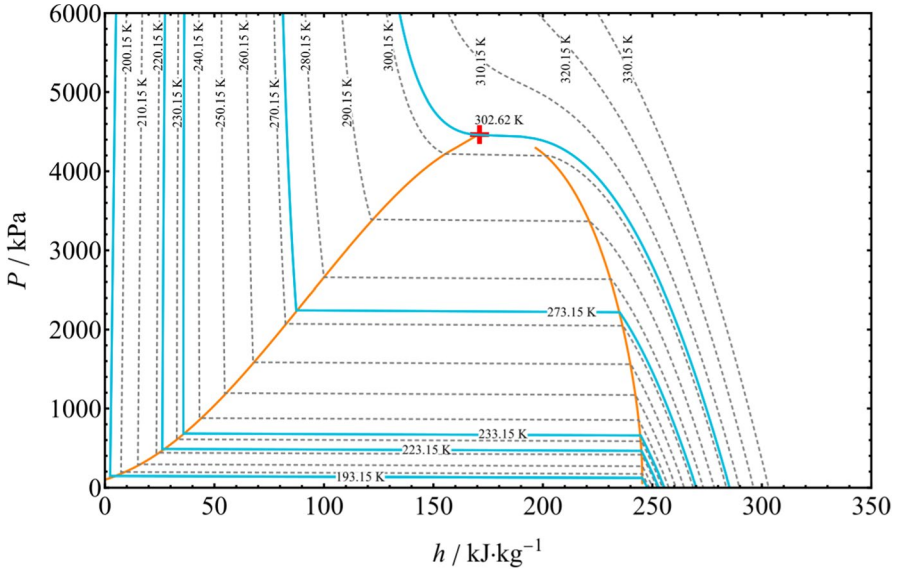

Fig. 8 Pressure–enthalpy (P–h) diagram for R-1132a constructed using the P-R EoS

liquid-phase PvT properties. Table 19 provides the AAD with respect to pressure or density when either the specific correlation is used or the P-R EoS is applied.

Through the observation of the AAD values in Table 19, it is evident that the P-R EoS cannot achieve the same precision as the individual correlations. The P-R EoS also faces limitations when predicting the liquid-phase behavior. This is an ingrained characteristic of the P-R EoS which could be improved upon by applying the volume translation to the P-R EoS. Even though the AAD for the specific correlations is smaller, the P-R EoS is capable of providing an overall representation of R-1132a as a single equation. This makes it useful and easier for practical applications. By utilizing the P-R

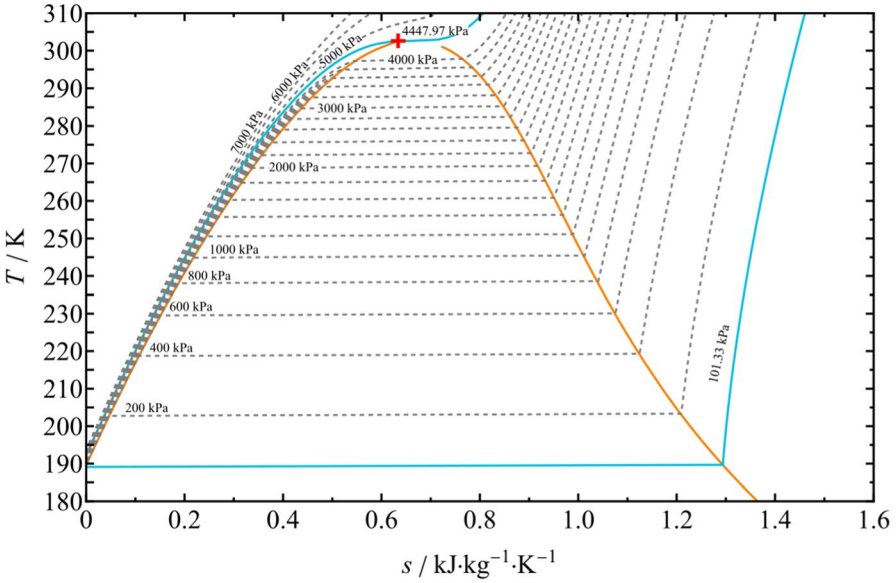

Fig. 9 Temperature–entropy (*T*–*s*) diagram for R-1132a constructed using the P-R EoS

EoS, the *P*–*h* diagram and the *T*-*s* diagram for R-1132a are constructed and provided in Figs. 8 and 9. Additionally, several properties of R-1132a are summarized in table form for specific temperatures and pressures and included in the supplementary files.

The *P*–*h* diagram shows the saturation curves for R-1132a and the enthalpy at the critical temperature calculated using the P-R EoS. The isotherms from 193.15 K to the critical temperature (302.62 K) and 330.15 K are shown as well.

The *T*-*s* diagram shows the saturation curve for R-1132a and the entropy at the critical temperature calculated using the P-R EoS. The isobaric lines from the atmospheric pressure of 101.325 kPa to the critical pressure (4447.97 kPa) and 7000 kPa are provided as well.

4 Conclusions

The interest in the HFO refrigerant R-1132a has been increasing due to its potential as an alternative for the high GWP HFC R-23, and this work presented renewed measurements of its thermodynamic properties. The new critical temperature, density and pressure for R-1132a were measured and compared to previous values from the literature. The new measurements can be considered as improved measurements with lower uncertainties. The saturation pressures of R-1132a were measured using the isochoric method, and a correlation was optimized. Measurements from an independent apparatus were used to verify this correlation and additional comparisons to results in the literature were carried out. The new measurements show good reproducibility among different isochoric apparatuses; they show some acceptability with the results of Tomassetti and di Nicola toward the lower temperatures of 230 K,

while the results by Low increasingly deviate toward both the low temperatures and critical temperature; the results by Otto and Thomas near the new critical point match well with the present measurements.

The saturated liquid densities and saturated vapor densities were determined using the inflection points of the isochores and with the disappearance of the meniscus level using the critical point apparatus. These coexistence data were used to optimize a correlation for the liquid- and vapor-phase saturated densities and they were compared to results from the literature. Data obtained from the *PvT* inflection points and the direct visual observations were comparable to each other. The saturated liquid densities were similar to values from the literature and showed relatively small deviations; the saturated vapor-phase data showed slightly higher deviations, but were similar in values to data obtained from the literature. Determining the inflection points through *PvT* data is an important method for increasing the range of obtainable saturated density data.

Next the *PvT* properties in the single-phase regions were correlated using the virial EoS truncated at the third term for the superheated vapor-phase data and using a Tait correlation for the subcooled liquid region data. These correlations were also compared to previous results from the literature. For the superheated vapor phase, the optimized temperature functions of the second virial coefficient *B* showed good consistency with results from Koschine and Lehmann as well as Dymond et al. The third virial coefficient *C* also showed the expected trend with temperature, with a peak occurring close to the new critical point, and was similar to the results from Koschine and Lehmann as well. The present isochores were all well represented by the virial EoS. The relative deviations for the lower density isochores from Tomassetti and di Nicola showed a similar distribution to present data. The data by Mears et al. showed slightly larger deviations, which could possibly be caused by the extraction of data from graphical sources. The liquid-phase *PvT* data on the other hand showed somewhat larger deviations for the second isochore nearer to the critical density, which could be more difficult to represent due to the closeness to the supercritical region. The liquid data by Otto and Thomas were fairly scattered, but showed similar deviations to the present work.

Finally, the P-R EoS was used to predict all of the above property measurements as a generalized representation of R-1132a. The P-R EoS showed difficulty in representing liquid-phase properties. Though the AAD was larger when compared to the specific correlations presented above, the P-R EoS was additionally used to determine the *P–h* and *T-s* diagrams. Several thermodynamic properties of R-1132a determined using the P-R EoS are provided in the supplementary material in table form.

Supplementary Information The online version contains supplementary material available at https://doi.org/10.1007/s10765-023-03184-4.

Acknowledgments The authors are grateful to Daikin Industries Ltd. for furnishing the high-purity sample of R-1132a.

Author Contributions UP wrote the manuscript, prepared the figures, conducted the experiments and analyzed the data. KM conducted the experiments and analyzed the data. NS reviewed the manuscript and analyzed the data. KT wrote the manuscript, conducted the experiments and analyzed the data. YH conducted the experiments, analyzed the data, reviewed the manuscript, prepared the samples and supervised the work. The manuscript was written through contributions of all authors. All authors have given approval to the final version of the manuscript. These authors contributed equally.

Funding Not applicable.

Declarations

Competing interest The authors declare that they have no known competing financial interests or personal relationships that could have influenced the work reported in this paper.

Ethical Approval Not applicable.

References

1. European Environment Agency, *Fluorinated Greenhouse Gases 2020* (Luxembourg, 2020).
2. P. Denzinger, *COVID-19 and How to Establish a Sustainable and Climate Resilient Vaccine Cold Chain - Green Cooling Initiative* (Eschborn, 2021).
3. P. Giménez-Prades, J. Navarro-Esbrí, C. Arpagaus, A. Fernández-Moreno, A. Mota-Babiloni, Renew. Sustain. Energy Rev. **167**, 14 (2022)
4. A. Mota-Babiloni, M. Mastani-Joybari, J. Navarro-Esbrí, C. Mateu-Royo, Á. Barragán-Cervera, M. Amat-Albuixech, F. Molés, Int. J. Refrig. **111**, 147 (2020)
5. R. Low, Refrig. Sci. Technol. Part. **F1476**, 504 (2018)
6. M.O. McLinden, M.L. Huber, J. Chem. Eng. Data **65**, 4176 (2020)
7. V. Webster, I. Saxena, R. E. Low, and C. J. Seeton, in *Int. Refrig. Air Cond. Conf.* (Purdue e-Pubs, 2022), p. 2452.
8. M. L. Macneill, C. J. Seeton, and R. E. Low, in *Int. Refrig. Air Cond. Conf.* (Purdue e-Pubs, 2022), p. 2446.
9. T. Winkler, M. Cop, R. B. Barta, and U. Hesse, in *Int. Refrig. Air Cond. Conf.* (Purdue e-Pubs, 2022), p. 2330.
10. U. Perera, K. Thu, N. Sakoda, and Y. Higashi, Trans. Japan Soc. Refrig. Air Cond. Eng. (2022).
11. W.H. Mears, R.F. Stahl, S.R. Orfeo, R.C. Shair, L.F. Kells, W. Thompson, H. McCann, Ind. Eng. Chem. **47**, 1449 (1955)
12. J. Otto, W. Thomas, Int. J. Heat Mass Transf. **7**, 41 (1964)
13. A. Koschine, J.K. Lehmann, Meas. Sci. Technol. **3**, 411 (1992)
14. J. H. Dymond, K. N. Marsh, R. C. Wilhoit, K. C. Wong, and M. D. Frenkel, in *Landolt-Börnstein Numer. Data Funct. Relationships Sci. Technol. - New Ser.*, edited by M. Frenkel and K. N. Marsh (Springer, Berlin 2002), pp. 121–122
15. S. Tomassetti, G. Di Nicola, Fluid Phase Equilib. **533**, 112939 (2021)
16. S. Tomassetti, G. Di Nicola, C. Kondou, Int. J. Refrig. **133**, 172 (2022)
17. K. Thu, U. A. Perera, K. Miyane, N. Sakoda, and Y. Higashi, Int. J. Thermophys. Pre-public, (2023).
18. R. Akasaka, Y. Kayukawa, Y. Higashi, Int. J. Thermophys. **43**, 1 (2022)
19. U.A. Perera, N. Sakoda, T. Miyazaki, K. Thu, Y. Higashi, Int. J. Refrig. **135**, 148 (2022)
20. S. Okazaki, Y. Higashi, Y. Takaishi, M. Uematsu, K. Watanabe, Rev. Sci. Instrum. **54**, 21 (1983)
21. Y. Higashi, Int. J. Refrig. **17**, 524 (1994)
22. N. Sakoda, U.A. Perera, K. Thu, Y. Higashi, Int. J. Refrig. **63**, 3818 (2022)
23. K.S. Pitzer, J. Am. Chem. Soc. **77**, 3427 (1955)
24. U.A. Perera, K. Thu, N. Sakoda, M. Kozue, Y. Higashi, J. Chem. Eng. Data **67**, 2182 (2022)
25. W. Pentermann, W. Wagner, J. Chem. Thermodyn. **10**, 1161 (1978)
26. D.Y. Peng, D.B. Robinson, Ind. Eng. Chem. Fundam. **15**, 89 (1976)
27. J.S. Brown, Int. J. Refrig. **30**, 1319 (2007)

28. B. E. Poling, J. M. Prausnitz, and J. P. O'Connell, *The Properties of Gases and Liquids*, 5th ed. (McGraw-Hill, 2004).
29. Wolfram, Mathematica. (Wolfram 2023), https://www.wolfram.com/mathematica/. Accessed 21 February 2023
30. NIST Chemistry Web Book, Ethene,1,1-difluoro-. (NIST 2021), https://webbook.nist.gov/cgi/cbook.cgi?Name=1%2C1-difluoroethene&Units=SI. Accessed 21 February 2023
31. M. S. Owen and A. Eltalouny, *Update on New Refrigerants Designations and Safety Classifications* (2022).